Adsorption and photo-oxidation of acetaldehyde on TiO_2 and sulphate modified TiO_2: Studies by in situ FTIR spectroscopy and micro-kinetic modelling

Z. Topalian, B. I. Stefanov, C. G. Granqvist and L. Österlund*

Department of Engineering Sciences, The Ångström Laboratory, Uppsala University,
P.O. Box 534, SE-751 21 Uppsala, Sweden.

*) Corresponding author

Abstract

Adsorption and photocatalytic oxidation of acetaldehyde have been investigated on TiO_2 and sulphate-modified TiO_2 films (denoted SO_4–TiO_2). In situ Fourier transform infrared spectroscopy was used to study surface reactions as a function of time and number of experimental cycles. Spectral analysis and micro-kinetic modelling show that crotonaldehyde formation occurs spontaneously on TiO_2 but is impeded on SO_4–TiO_2, where instead acetaldehyde desorption is significant. Photo-oxidation yields significant amounts of formate on TiO_2, and was identified as the rate-determining step and associated with site blocking. Significantly smaller amounts of formate were observed on SO_4–TiO_2, which is due to the acidity of this surface resulting in weaker bonding of aldehyde and carboxylate intermediate species. Our results are of considerable interest for applications to photocatalytic air purification and to surfaces with controlled wettability.

Keywords. Acetaldehyde, TiO_2, photocatalysis, in situ Fourier transform infrared spectroscopy, micro-kinetic modelling, acid-base properties, surface functionalization.

1. Introduction

Titanium dioxide (TiO_2) is a wide band gap semiconducting oxide which has been extensively studied for a variety of applications such as biomaterials, optical coatings, chemical sensors, and catalysis [1–5], many of which lie in the realm of "green nanotechnology" [6]. In particular, photocatalytic removal of volatile organic compounds has been highlighted as an efficient and cost-effective method to clean indoor air [7]. Aldehydes are common indoor air pollutants and are released from many different sources such as synthetic materials, surface coatings and building insulation materials. There are several studies on the oxidation of acetaldehyde and other aldehydes in the literature [8], and the oxidation mechanism of acetaldehyde has been reviewed in detail [8–11]. However, there is no general agreement on the reaction pathways for acetaldehyde photo-oxidation on TiO_2; it has been reported to occur through several parallel reaction pathways, and numerous intermediates—including formate, acetic acid and formaldehyde—have been identified [10, 11]. It has also been shown that the adsorption of acetaldehyde on TiO_2 is immediately followed by its condensation to crotonaldehydeat room temperature [12], and that 3-hydroxybutanal is a short-lived intermediate [13]. Similar condensation reactions have been documented also on other oxide surfaces such as CeO_2, ZrO_2 and MgO [14, 15].

Large efforts have been made to modify the acid–base surface properties of oxides used for heterogeneous catalysis in order to control and enhance selectivity [16, 17]. Specifically the acid–base characteristics of oxide surfaces influence the activation of adsorbed molecules and can modify the rates of competitive reaction pathways. In low temperature heterogeneous catalysis, with photocatalysis being one example, site-blocking and concomitant catalyst deactivation by strongly bonded intermediate products frequently take place, and these processes eventually deteriorate the overall efficiency of the catalyst [18]. It is well-known that desorption is usually a rate-determining step in photocatalytic reactions, and it follows that modification of the acid–base surface properties of oxide-based photocatalysts may be a viable way to improve their sustained activity. TiO_2 has amphoteric surface chemical properties, which can be exploited for selective acid–basic surface reactions, for example in the Claus reaction [19], i.e., the catalytic removal of sulphur from acidic gases containing hydrogen sulphide. In a modified form this reaction includes partial oxidation of H_2S to SO_2 as a first step, which is then followed by oxidation to water and sulphur. Deactivation occurs on γ-Al_2O_3 catalysts because of sulphur deposits. In contrast, TiO_2 catalysts promote the

oxidation of H_2S and SO_2 and simultaneously avoid deactivation via sulphur accumulation. The latter property is due to reactions between lattice oxygen in TiO_2 and adsorbed sulphur, which replenishes the catalyst in an oxidizing atmosphere [20].

We have previously shown that photo-fixation of SO_2 on nanocrystalline TiO_2 at elevated temperature in an oxidizing atmosphere leads to covalent bonding of SO_2 to oxygen vacancy sites [21], which are subsequently oxidized to sulphate species [22]. These sulphate moieties change the acid–base properties of TiO_2, which results in e.g. oleophobic surface properties [22, 23] of much interest for keeping exposed surfaces clean and hygienic. One purpose of the present work is to explain the origin of this oleophobic phenomenon in detail. The present paper reports on the elementary reaction steps for adsorption and photocatalytic oxidation of acetaldehyde on pristine and SO_2-modified nanocrystalline anatase TiO_2. We utilize in situ infrared spectroscopy and micro-kinetic modelling and show that changes in the acid–base surface properties of the SO_2-modified TiO_2 result in modified surface reaction pathways and weaker bonding of carboxylate intermediates. These findings are of much interest for applications to photocatalytic air purification, oleophobic surfaces, etc.

2. Materials and Methods

2.1 Material preparation

Thick and porous TiO_2 films were prepared from a paste containing TiO_2 nanoparticles (DSL 18NR-T from Dyesol, Queanbeyan, Australia). The bulk density of the TiO_2 particles was determined by the use of a He-pycnometer (AccuPyc 1340 from Micrometrics, Norcross, GA, USA), and was determined to be 3.71 g cm^{-3} which should be compared with the value for bulk TiO_2 anatase (3.90 g cm^{-3}). This yields a powder porosity of 82.5%. The paste was applied on CaF_2 substrates by the doctor-blading technique. The samples where dried in a fume hood for 24 h and were then annealed in air at successively increasing temperature: at 180, 320 and 390 °C for 10 min at each temperature step, and finally at 450 °C for 1 h. Heat treatments were performed in an oven with a temperature control better than ±2 °C. The film thickness was d_f ~ 6.5 μm, as determined by surface profilometry (Dektak XT Advance from Bruker, Tucson, AZ, USA).

Surface modification of the TiO_2 films with SO_2 was performed in a dedicated reaction cell as described elsewhere [23]. Briefly, we used a flow of synthetic air containing 50 ppm of SO_2 passing over TiO_2 films kept at 200 °C during simultaneous UV irradiation. This treatment resulted in covalent attachment of SO_2 molecules to oxygen lattice vacancy sites at the TiO_2 surface [22]. The adsorbed SO_2 was further oxidized to SO_4^{2-} species in the reaction cell and yielded a surface which is more acidic than the pristine TiO_2 surface. The treated films are denoted SO_4–TiO_2 and are understood to comprise nanocrystalline anatase TiO_2 with SO_4 surface species.

2.2 Materials characterization

Structural studies were made by grazing-incidence X-ray diffraction (GIXRD), using a Siemens D5000 diffractometer operating with CuK_α radiation at a grazing angle of incidence θ equal to one degree. The mean grain size D was estimated from Scherrer's formula, $D = K\lambda/\beta \cos\theta$ where K is a dimensionless constant (here assumed to be 0.9, which is appropriate for spherical grains), 2θ is the diffraction angle, λ is the X-ray wavelength (1.5406 Å), and β is the full width at half maximum (FWHM) of the diffraction peak. Standard data were used to identify the diffraction peaks for TiO_2 [24]. The GIXRD measurements showed that films of pristine TiO_2 and SO_4–TiO_2 contain only the anatase phase. By applying Scherrer's formula to the strongest diffraction peak (the <101> reflection), we found the mean crystallite size to be 11.5 and 12.6 nm for TiO_2 and SO_4–TiO_2 films, respectively.

Elemental surface compositions of the films were determined by X-ray photoelectron spectroscopy (XPS) by use of a PHI Quantum 2000 ESCA system (PHI, Chanhassen, MN, USA) with a focusing X-ray monochromatic AlK_α radiation source. The system was equipped with a low-energy electron flood gun and a charge neutralization gun. Survey spectra were collected using a pass energy of 187 eV with an energy resolution of 0.8 eV per step. The binding energy (BE) scale was calibrated against the aliphatic C 1*s* peak at BE = 284.8 eV due adventitious carbon on the surface. The oxidation state of the sulphur atoms was determined to be +6 [22]. The sulphur content in the SO_4–TiO_2 samples was estimated to be 1.98 ± 0.1 at.% and was calculated as the ratio of the atomic concentration of S and Ti determined from XPS survey scans.

The penetration depth of light in the films, d_p, was calculated from the measured absorption coefficient $\alpha(\lambda)$ by use of the relation $d_p(\lambda) = \alpha(\lambda)^{-1}$. Specific data were obtained from spectrophotometric recordings of reflectance and transmittance according to

$$\alpha(\lambda) = d_f^{-1} \ln\left(\frac{1-R_{cor}(\lambda)}{T_{cor}(\lambda)}\right) , \quad (1)$$

where $R_{cor}(\lambda)$ and $T_{cor}(\lambda)$ are the corrected values of the total reflectance and transmittance, respectively, obtained according to methods discussed elsewhere [23]. Using eqn. 1, d_p was found to be ~38 μm at λ = 370 nm, which is the wavelength of our LED light source and is close to the absorption edge of TiO_2. Since d_f = 6.5 μm, this means that $d_f << d_p$ implying that the film, to a good approximation, can be regarded as homogeneously irradiated in the experiments.

2.3 In situ FTIR spectroscopy

Fourier transform infrared (FTIR) spectroscopy measurements were performed in a vacuum-pumped spectrometer (Bruker IFS66v/S, Ettlingen, Germany) equipped with a liquid nitrogen cooled narrow-band HgCdTe detector. All measurements were carried out in a custom-modified transmission reaction gas cell, which allows for in situ reaction studies at controlled sample temperatures with simultaneous FTIR spectroscopy, gas dosing and light illumination in a controlled gas atmosphere as a function of reaction time, as described elsewhere [25]. Light irradiation was performed with a UV light emitting diode (LED) with an emission wavelength of 370 nm and a FWHM of 12 nm. The output from the LED source was 1.1 mW at the sample position, as measured with a calibrated thermopile detector (Ophir, North Andover, MA, USA), and hence the number of incident photons at λ = 370 nm was calculated to be N_{ph} = 2.05×10^{15} photon s^{-1}. The cross sectional area at FWHM of the light spot on the sample was measured to be A_{ph} = 0.086 cm^2. The number of photons absorbed by the film per unit area then becomes

$$N_v = N_{ph} \cdot \alpha \cdot d_f / A_{ph} = 4.03 \times 10^{15}\ photons \cdot cm^{-2} \cdot s^{-1}. \quad (2)$$

Repeated FTIR spectra were recorded between 1000 and 4000 cm^{-1} as a function of irradiation time every 60 s with 4 cm^{-1} resolution and with each spectrum averaged over 138 scans. All spectra were smoothed with a Savitzky–Golay algorithm using a nine-point window. FTIR absorbance *A*' was determined from measured transmittance *T*, after appropriate base line corrections, from the relation $A' = -log(T)$. FTIR spectra were obtained with the samples kept at room temperature in 100 ml min^{-1} gas flow. Prior to each measurement, the samples were cleaned in the reaction cell at 200 °C for 15 min in synthetic air and were subsequently cooled to the working temperature for data acquisition.

The adsorption and photo-reaction of acetaldehyde were studied as a function of time and experimental cycle. Each cycle consisted of the following steps (see Fig. 2a below): First, the samples were exposed to 50 ppm acetaldehyde for 12 min ("dosing period"), synthetic air was then flowed through the reaction cell for 10 min ("purging period"), and finally the samples were UV irradiated for 30 min ("UV period"). In all measurements, the FTIR background was collected on a clean sample in a flow of synthetic air at the desired sample temperature prior to gas dosing. All samples were placed with the film side facing the IR detector, and UV irradiation was performed at 30° angle of incidence in order to prevent light from being scattered into the spectrometer's detector compartment.

The saturation coverage, N_{sat}, of acetaldehyde on the surface of TiO_2 is expressed as $N_{sat} = N_{site} \cdot A_V$, where $N_{site} \approx 5 \times 10^{14}$ molecules cm^{-2} and is the number of adsorption sites available on TiO_2 surface (101). Here N_{site} is defined as the number of primitive unit cells on the (101) surface, and A_V is the total surface area enclosed within the volume *V* with mass *m* and is calculated from $A_V = A_{BET} \cdot m$, where A_{BET} is the Brunauer-Emmett-Teller (BET) specific surface area of the TiO_2 powder, which previously has been measured to be A_{BET} = 68.8 m^2g^{-1} [26]. Furthermore, *m* is determined from the density of the powder as $m = V \cdot \rho_{powder}$. The density ρ_{powder} was estimated to be ~0.65 $g \cdot cm^{-3}$ by weighting and measuring a volume of TiO_2 powder prepared from the same paste and using the same annealing procedure as described in section 2.1. The volume of the porous film per unit area is calculated as $V/A = d_f$. We thus obtain the saturation coverage per unit area as

$$n_{sat} = \frac{N_{sat}}{A} = N_{site} \cdot A_{BET} \cdot d_f \cdot \rho_{powder} = 1.45 \times 10^{17} molec. \cdot cm^{-2} = 0.24\ \mu mol \cdot cm^{-2} \quad (3)$$

The quantum yield, $\phi_{i\to j}$, for converting species *i* into species *j* is defined as

$$\phi_{i\to j}(\%) = \frac{\#photoconverted\ molecules\ cm^{-2}s^{-1}}{\#absorbed\ photons\ cm^{-2}s^{-1}} \times 100 \equiv \frac{K_{i\to j}}{N_v} \times 100 = \frac{n_{sat} \cdot k_{i\to j}}{n_{ph} \cdot \alpha \cdot d_f / A_{ph}} \times 100, \quad (4)$$

where $k_{i\to j}$ is the rate of photo-conversion in units [s^{-1}] and $K_{i\to j} = n_{sat} \cdot k_{i\to j}$ is the reaction rate constant in units of $\mu mol \cdot cm^{-2} \cdot s^{-1}$.

2.4 Data processing and micro-kinetic modelling

The procedure for extracting quantitative data from FTIR absorbance data is complicated for two reasons: First, acetaldehyde reacts immediately upon adsorption on the pristine TiO_2 surface and undergoes an aldol condensation reaction, and, secondly, the absorbance of the TiO_2 samples changes during UV illumination and shifts the background in the FTIR spectra. This shift is related to the excitation of long-lived IR absorbing states below the conduction band of TiO_2, which become populated upon UV irradiation [27].

To correct for the changing background, we used integrated data for the adsorbing species (acetaldehyde) as follows: Prior to the first UV irradiation cycle, the acetaldehyde coverage decreases due to the aldol condensation reaction. This second-order reaction was fitted by the equation

$$\frac{1}{\theta_A} = \frac{1}{\theta_{A_0}} + kt, \quad (5)$$

where θ_A and θ_{A_0} are the coverages of acetaldehyde at times *t* and zero, respectively, and *k* is the second-order rate constant. The fit was then extrapolated through the first photocatalytic

cycle, where the largest shift of the background occurs, and this extrapolated fit was subtracted from the experimental data, leaving only what we assume to be a rigid background shift due to the changed IR reflectivity of the TiO_2 film. Subsequently, this up-shift was fitted with the power-law relation

$$I = at^b, \tag{6}$$

where I is the background intensity, and a and b are constants.

This procedure is illustrated in Fig. 1 with regard to the integrated FTIR absorption bands between 1680 and 1708 cm^{-1} for acetaldehyde on TiO_2. Equation (6) presumes that the states generated by the initial UV excitation are sensitive to IR radiation so that a weak and gradual drift of the background takes place throughout the duration of the IR illumination.

After background correction as described above, the FTIR absorbance bands of the main adsorbates were normalized and scaled to ensure mass balance. It was assumed that two molecules of CH_3CHO on a pristine TiO_2 surface yield one molecule of crotonaldehydeand four molecules of formate; this surmise was adopted in order to compensate for the unknown IR cross sections of adsorbed acetaldehyde, crotonaldehyde and formate. The normalization was done for acetaldehyde and crotonaldehyde against their saturation coverages, which was calculated from a best fit of the FTIR absorbance data in the first cycle to an ideal Langmuir adsorption isotherm according to

$$\theta_A = \theta_{A_0} + A_{sat}(1 - e^{-kt}), \tag{7}$$

where A_{sat} is a constant with the physical meaning of a maximum site occupation of species A (*cf.* Fig. 1). The formate absorbance data were normalized against its maximum value. Absolute coverages, N_A, were then obtained from $N_A = n_{sat}\theta_A$.

The R statistical computing package [28] was use for detailed analyses of the FTIR spectra. Infrared absorbance data were extracted from background-corrected FTIR spectra by numerical integration of selected peaks using Simpson's rule. Micro-kinetic modelling of the extracted absorbance bands was performed with the Simecol package [29]. The Runge–Kutta forth order integration solver (rk4), as implemented in to the deSolve package, was used for least-square fitting of model parameters to experimental data [30].

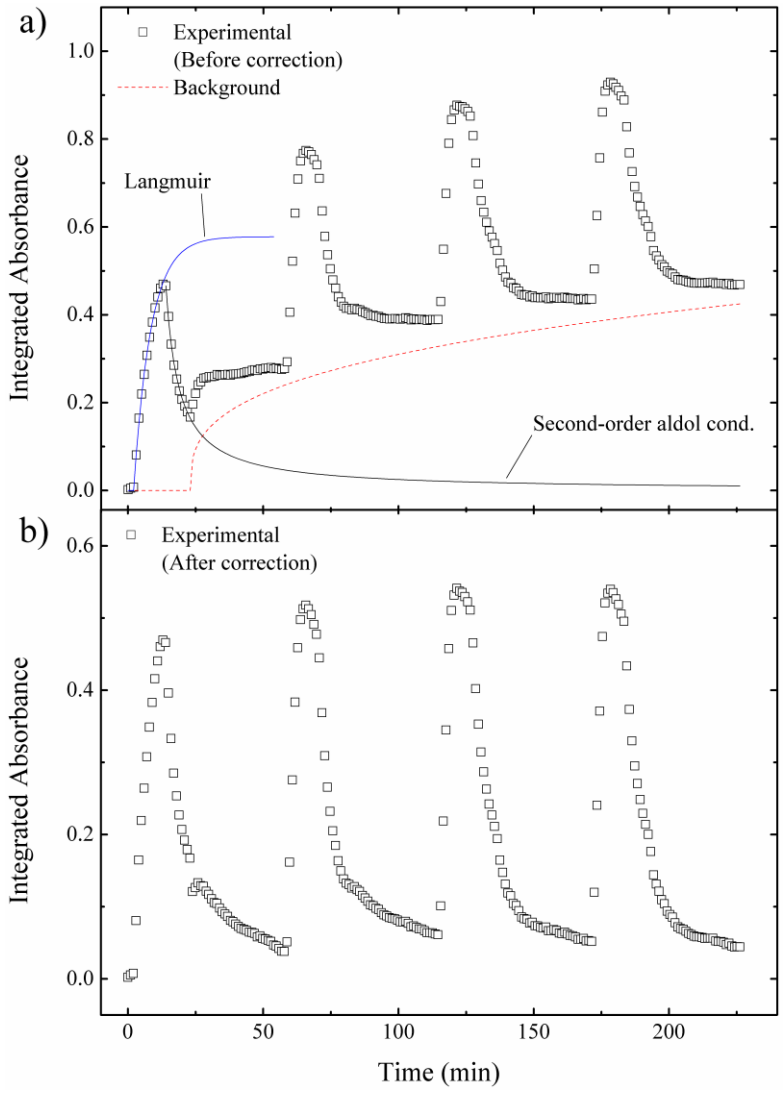

Figure 1. Integrated FTIR absorbance bands between 1680 and 1708 cm^{-1} for acetaldehyde on a TiO_2 surface without (panel a) and with (panel b) baseline corrections. The blue solid curve shows the fit of a Langmuir adsorption isotherm to the first cycle of acetaldehyde adsorption. The black solid line shows the best fit to the second-order aldol condensation reaction. The red dashed curve shows the baseline curve obtained by the procedure described in the text.

Table 1. Vibrational frequency and mode assignment of IR bands on TiO_2 and sulphated TiO_2

Sample	Frequency (cm^{-1})	Assignment
TiO_2	1733	ν(C=O); H-bonded CH_3CHO
	1720	ν(C=O); coordinated $CO_2^{\delta-}$
	1693	ν(C=O); Ti-O=$CHCH_3$
	1677	ν(C=O) ; V_O-O=$CHCH_3$
	1653	ν(C=O); Ti-O=$CH(CH)_2CH_3$
	1628	ν(C=C); Ti-O=$CH(CH)_2CH_3$
	1580	ν_a(C-O); asymmetric O-C-O stretching in coordinated $HCOO^-$
	1421	$\delta(CH_3)$ d-deformation; Ti-O=$CHCH_3$
	1376	δ(CH) bending; Ti-O=$CHCH_3$ δ(C-H); $HCOO^-$
	1355	$\delta(CH_3)$ s-deformation; Ti-O=$CHCH_3$ ν_s(C-O); symmetric O-C-O stretching in $HCOO^-$
	1220	ν(C-O); coordinated $CO_2^{\delta-}$
	1168	ν(C-C); Ti-O=$CH(CH)_2CH_3$
	1129	ν(C-C); Ti-O=$CHCH_3$
	1099	$\rho(CH_3)$; Ti-O=$CH(CH)_2CH_3$
SO_4-TiO_2	1699	ν(C=O); SO_4 coordinated $CHOCH_3$
	1684	ν(C=O); SO_4 coordinated $CHOCH_3$
	1655	ν(C=O); Ti-O=$CH(CH)_2CH_3$
	1553	ν_a(C-O); asymmetric O-C-O stretching; coordinated $HCOO^-$
	1418	$\delta(CH_3)$ d-deformation; Ti-O=$CHCH_3$
	1357	δ(CH) bending; Ti-O=$CHCH_3$
	1313	$\delta(CH_3)$ s-deformation; Ti-O=$CHCH_3$
	1221	ν(C-O); coordinated $CO_2^{\delta-}$
	1137	ν(C-C); Ti-O=$CHCH_3$

3. Results and Discussion

3.1 In situ FTIR Spectroscopy

3.1.1 TiO_2

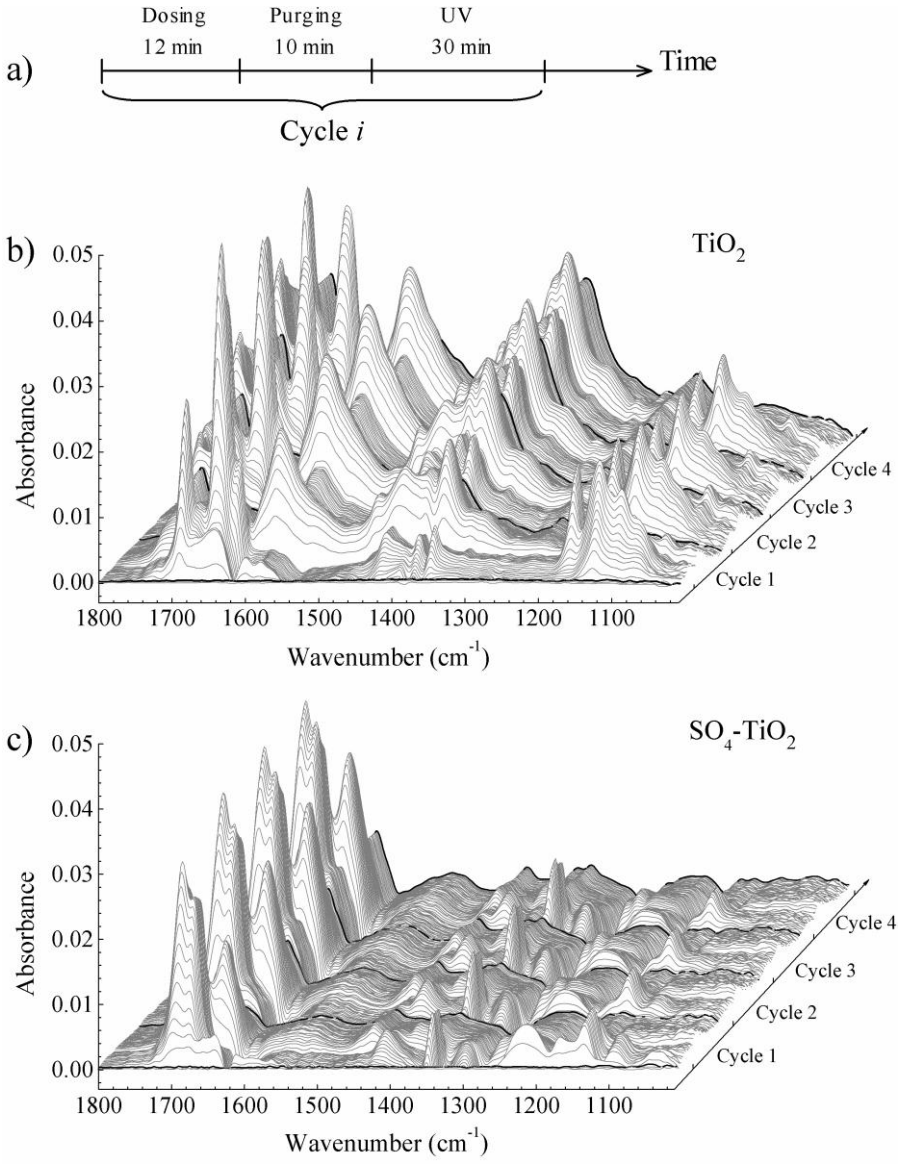

Figure 2. Panel (a) is a schematic representation of the experimental procedure used in the in situ FTIR experiments. Panels (b) and (c) show absorbance spectra acquired (bottom to top) as a function of time and consecutive cycle number on films of TiO_2 and SO_4–TiO_2, respectively. The first two bottom spectra in panels (b) and (c) were recorded in synthetic air prior to acetaldehyde gas admission.

Figure 2b shows a "three-dimensional" survey plot summarizing in situ FTIR spectra on TiO_2 as function of cycle number, and Fig. 3a shows the same data in an ordinary two-dimensional

diagram reporting detailed spectral changes occurring after acetaldehyde adsorption, subsequent purging in synthetic air, and UV irradiation.

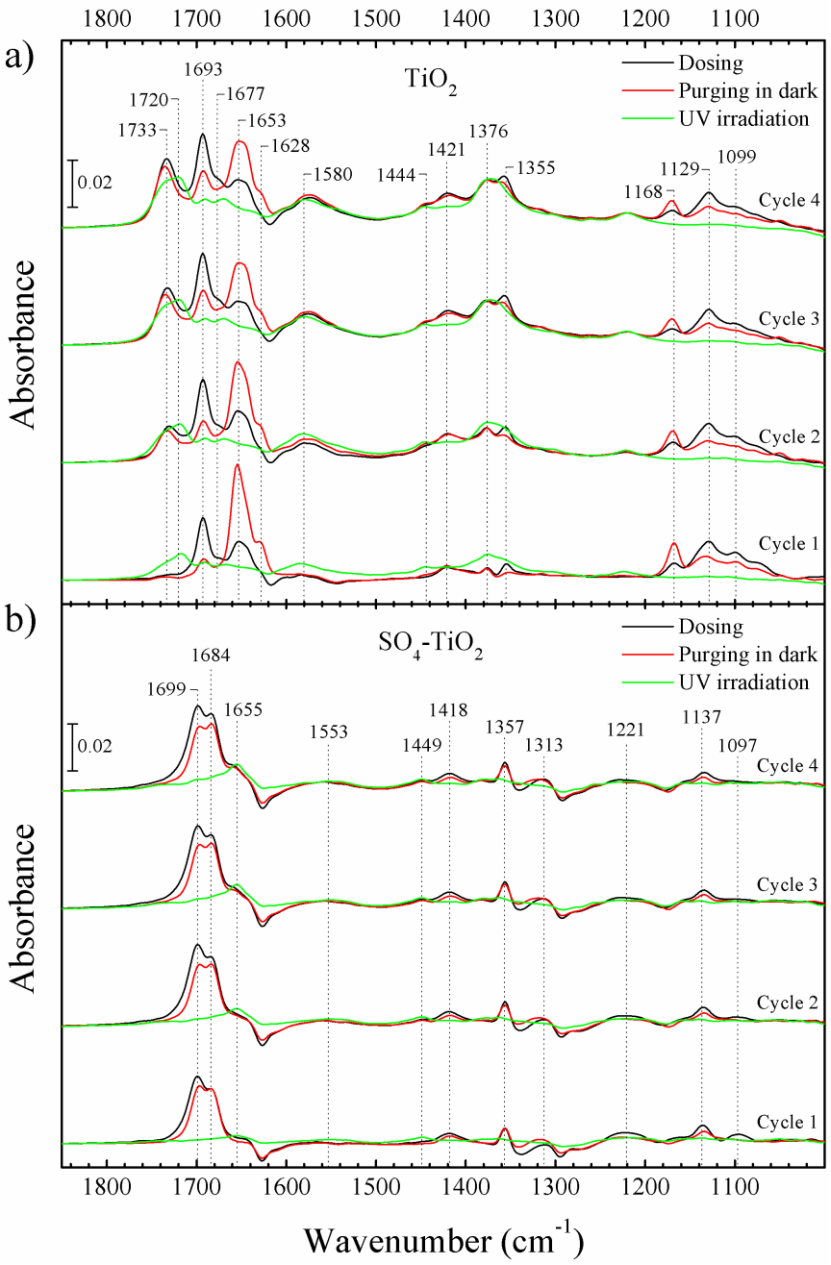

Figure 3. In situ FTIR spectra obtained after dosing with 50 ppm acetaldehyde (black curves), after subsequent purging in synthetic air (red curves), and after UV irradiation (green curves) for all four experimental cycles on films of TiO_2 (panel a) and SO_4–TiO_2 (panel b), respectively. The major band at 1653 cm^{-1} is due to croton aldehyde. Carbonyl bands due to acetaldehyde are located between 1677 and 1699 cm^{-1}.

It can be seen that acetaldehyde adsorption results in the formation of a carbonyl peak at 1693 cm^{-1}, characteristic of the acetaldehyde ν(C=O) vibration, along with weaker bands at 1653,

1421, 1376, 1355, 1168, 1129 and 1099 cm^{-1}. A compilation of the vibrational frequencies and their mode assignment is listed in Table 1.

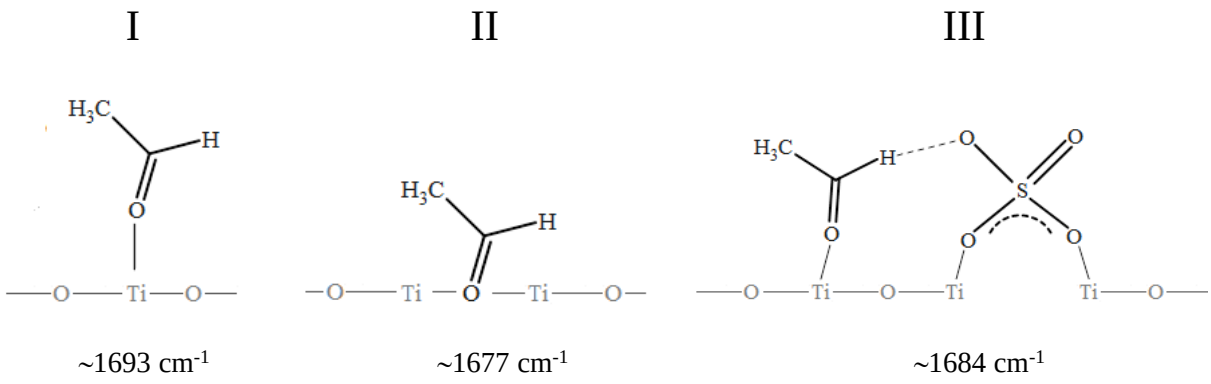

Figure 4. Schematic acetaldehyde adsorbate structures and associated ν(C=O) frequencies on TiO_2 and SO_4-TiO_2. On the sulphated surface all structures co-exist.

We note, however, that unambiguous assignment is obscured by the presence of condensation products (crotonaldehyde) and possible dimer formation. Support for the mode assignment can be found in literature as we discuss below, but lacking detailed knowledge of adsorption geometry and surface structure, the assignments presented in Table 1 should be regarded as tentative. The carbonyl peak is assigned to η^1-CH_3CHO bonded to Ti^{4+} sites through the carbonyl O atom (structure **I** in Fig. 4) [24], and the weak and broad shoulder at 1677 cm^{-1} is assigned to η^1-CH_3CHO bonded to oxygen vacancies (–C=O–V_O), or similar electrophilic defect sites (structure **II** in Fig. 4). It is observed that the strong peak at 1693 cm^{-1} decreases in intensity during purging of the reaction cell with synthetic air, while the intensity of the broad peak at 1653 cm^{-1} increases and a new band appears at 1628 cm^{-1}. The latter two bands are assigned to the ν(C=O) and ν(C=C) vibrations of crotonaldehyde and show that aldehyde condensation occurs on anatase TiO_2 at room temperature, which is consistent with results of previous studies [31, 32]. The band observed at 1168 cm^{-1} can be assigned to the C–C vibration mode in either of the aldehyde species. We can exclude that the band at 1629 cm^{-1} is due to water by a comparison with corresponding changes in the ν(OH) spectral region (not shown). Detailed inspection reveals that the peak centred at 1653 cm^{-1} actually is composed of two peaks which emerge after UV irradiation as seen in Fig. 5a, and a deconvolution of the

carbonyl band yields peaks centred at 1657 and 1643 cm^{-1}. It is evident from Fig. 5b that the peak at 1657 cm^{-1} decreases faster than the peak at 1643 cm^{-1} during prolonged UV irradiation. We note that a recent study [11] on the first step of photo-oxidation of acetaldehyde indicated two reactions, one fast and one slow, which is in good agreement with the results in Fig. 5.

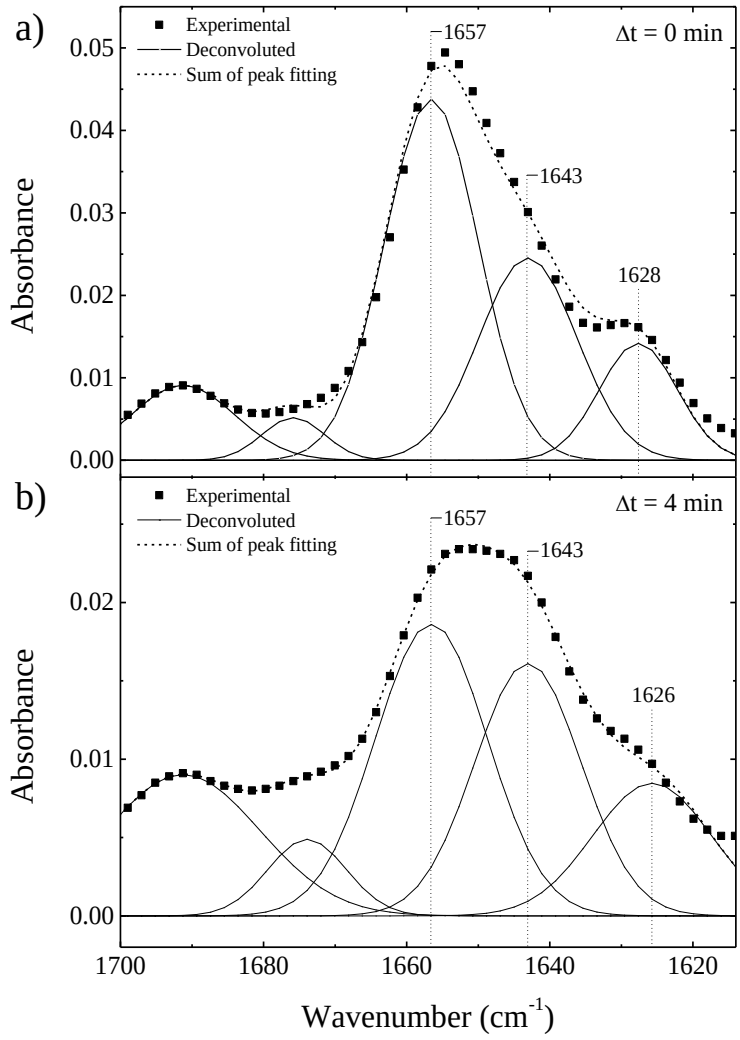

Figure 5. Dots show FTIR absorbance spectra in the carbonyl region on TiO_2 acquired before UV irradiation (panel a) and after 4 min of UV irradiation (panel b), respectively. The major bands at 1643 and 1657 cm^{-1} are due to croton aldehyde, and the band at ~1626 cm^{-1} represents small amounts of adsorbed water. Deconvoluted bands are shown as solid curves.

UV irradiation leads to a number of changes in the FTIR spectra: The carbonyl peak at 1653 cm^{-1} and the peak at 1168 cm^{-1} due to the C–C mode decrease simultaneously and there is an accompanying formation of a broad peak at 1580 cm^{-1}. The latter feature can be assigned to

asymmetric ν(OCO) vibrations due to coordinated formate and formate ions (see Ref. [33], and references therein). The peaks at 1376 cm^{-1} and 1355 cm^{-1} increase under UV irradiation; they can be attributed to δ(CH) and symmetric ν(OCO) vibrations, respectively, in formate. These bands overlap with the CH and CH_3 bending and deformation modes in acetaldehyde (Table 1). A peak at ~1444 cm^{-1} is also formed, probably due to formation of acetate [33]. After a couple of reaction cycles, it is found that an absorption band at ~1720 cm^{-1} evolves with time, accompanied by a weaker band at ~1220 cm^{-1}. These bands are due to the accumulation of chemisorbed $CO_2^{\delta-}$ (Table 1), which is known to bind strongly to oxygen vacancies on the surface [34, 35], and shows that photo-oxidation of acetaldehyde involves reactions with the lattice [10].

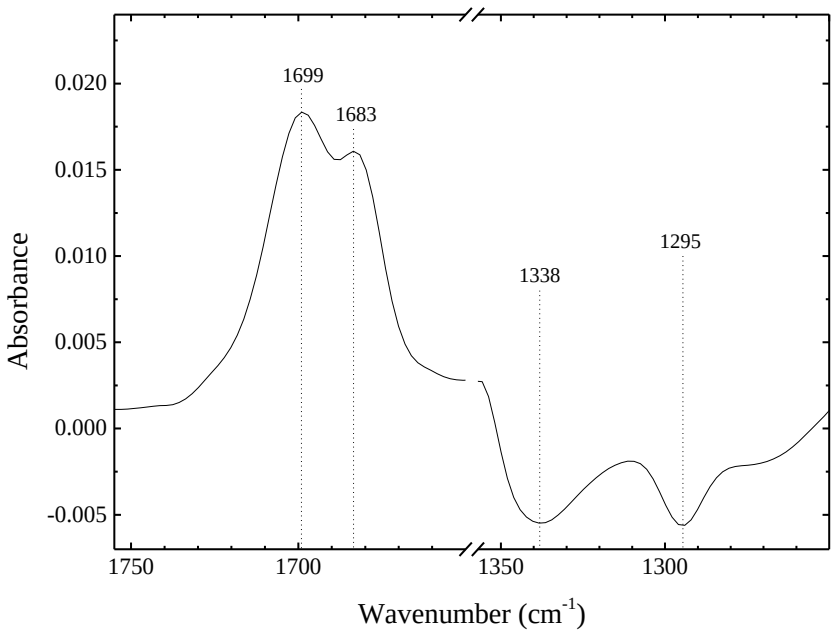

Figure 6. FTIR spectrum on SO_4–TiO_2 obtained immediately after acetaldehyde dosing in cycle 1.

3.1.2 SO_4–TiO_2

The SO_4-TiO_2 surfaces exhibit different FTIR spectra compared to the pristine TiO_2 surfaces, as can be seen from Figs. 2c and 3b, and comparing the data therein with those discussed above. Acetaldehyde adsorption of SO_4–TiO_2 leads to the appearance of a broad doublet carbonyl feature at 1699 and 1684 cm^{-1}. These new bands are tentatively attributed to adsorbed acetaldehyde interacting with surface sulphate species (e.g. structures **III** Fig. 4).

We also expect that ν(C=O) mode in η^1-CH_3CHO bonded to Ti^{4+} sites (structure **I** in Fig. 4), which is the dominant peak on TiO_2, contributes to the carbonyl bands. The latter assumption is qualitatively corroborated by a deconvolution of the carbonyl doublet band using three peaks, and it is rendered further support by the decrease of the modes in the 1290 to 1340 cm^{-1} region (see Fig. 6) and in the 1000 to 1200 cm^{-1} region (Fig. 3), and the formation of weak bands at 1418, 1357, 1313, 1221, 1137 and 1097 cm^{-1}, which signal chemical modifications of the coordinated sulphate species [22]. During purging, the only significant change is a decrease of the intense peak at 1699 cm^{-1}, which indicates acetaldehyde desorption. The spectra show that the condensation reaction and crotonaldehyde formation is significantly suppressed on SO_4-TiO_2, which can be seen by comparisons of the bands at 1655, 1628 and 1168 cm^{-1} in Fig. 3a and b, respectively.

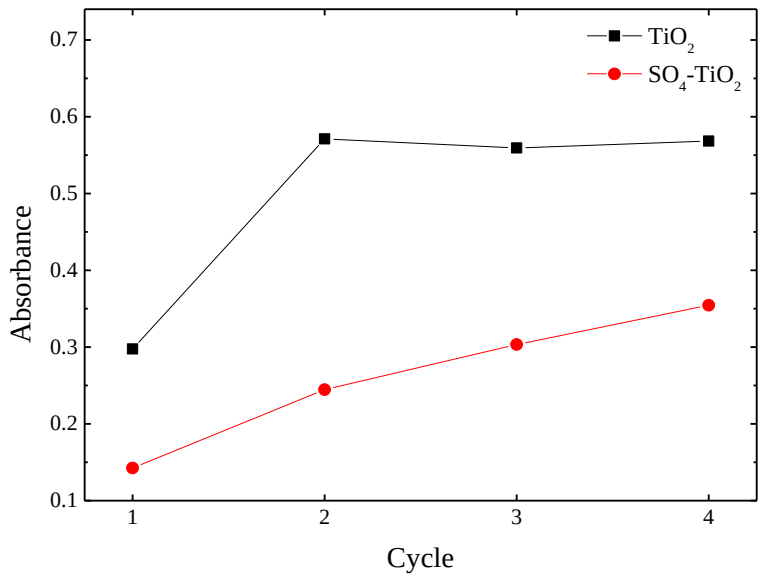

Figure 7. Ratio between integrated FTIR absorbance of accumulated formate and adsorbed acetaldehyde on TiO_2 and SO_4–TiO_2 films. FTIR absorbance data were integrated over 1506–1600 cm^{-1} and 1635–1756 cm^{-1} for formate [ν_a(OCO) band] and acetaldehyde [ν(C=O) band], respectively. Dots represent data, which are joined by lines for convenience.

UV irradiation leads to a rapid decrease of the peak at 1699 cm^{-1} and formation of a new peak at 1656 cm^{-1}. The occurrence of this latter feature during the photocatalytic reaction, and not during purging in synthetic air, suggests a different reaction on SO_4–TiO_2 than on pristine TiO_2. Clearly the condensation reaction is suppressed, and we conclude that interactions with the SO_4 surface groups stabilize the acetaldehyde monomers. Furthermore, the absorbance

bands in the 1500 to 1600 cm^{-1} region, due to carboxylate species, are very weak on SO_4–TiO_2, which suggests weaker interaction with the acidic SO_4–TiO_2 surface and significant desorption of aldehyde fragments. Finally, the absorbance band at ~1720 cm^{-1} is absent in the case of SO_4–TiO_2, which can be explained by the presence of sulphate species preferentially occupying oxygen vacancy sites [21] and preventing reactions due to CO_2 with the surface.

Comparing data taken on the pristine TiO_2 and on SO_4–TiO_2 surfaces after several cycle of adsorption and photo-oxidation, it is obvious that less carboxylate intermediates (formate) build up on the SO_4–TiO_2 surface. This is highlighted in Fig. 7, where the ratio of formate to acetaldehyde species is plotted as a function of cycle number. Carboxylate intermediates, and in particular formate (see Figs. 2b and c), which accumulated on the surface blocks adsorption sites and results in less acetaldehyde adsorption as a function of cycle number.

3.2 Surface reaction kinetics on TiO_2

Acetaldehyde photo-oxidation on TiO_2 is believed to occur through several parallel reaction pathways [36]. One of the major intermediates is reported to be formic acid, in the form of adsorbed formate [37], which is in good agreement with the results presented in previous sections. Experiments conducted under ultrahigh vacuum conditions on rutile single crystals show that photo-fragmentation of acetaldehyde leads to cleavage of the C–C bond and release of a $CH_3^{\bullet}$ radical [11]. This is consistent with formate formation under atmospheric conditions, since it is expected that $CH_3^{\bullet}$ radicals will be re-adsorbed on the surface to form methoxy groups and subsequently converted to formate species [31]. Other reported intermediates are acetic acid and formaldehyde as well as different condensation products such as 3-hydroxybutanal and crotonaldehyde [13, 38]. It is well known that crotonaldehydeforms spontaneously upon adsorption on anatase TiO_2 under standard conditions [13], as was also shown in Sec. 3.1.1.

A general reaction scheme, which accounts for the experimental findings in Section 3.1, can then be summarized as follows:

$$CH_3CHO_{ad} \rightarrow CH_3(CH)_2CHO_{ad} \rightarrow HCOO_{ad} + H_{ad} \rightarrow CO_2. \quad (8)$$

This scheme accounts for the major reactants and intermediates, namely adsorbed acetaldehyde, crotonaldehyde and formate. For simplicity, water formation and molecular oxygen are excluded in this generalized scheme, although they are important for the generation of oxidation agents through the initial photocatalytic reaction steps, *i.e.*, to produce hydroxyl and superoxide radicals [4].

The first step in reaction (8) is the adsorption of acetaldehyde on TiO_2; aldol condensation occurs at room temperature and yields croton aldehyde. The data presented in Sec. 3.1 showed that acetaldehyde adsorption is accompanied by crotonaldehyde formation, with their characteristic carbonyl bands located at 1693 and 1653 cm^{-1}, respectively, *i.e.*,

$$2A_g \xrightarrow{k_A^{ad}} 2A_{ad} \xrightarrow{k_{A\to B}^{DOSE}} B_{ad} + H_2O, \tag{9}$$

where *A* is acetaldehyde and *B* is crotonaldehyde, respectively, k_A^{ad} is the rate constant for adsorption, and $k_{A\to B}^{DOSE}$ is the rate constant for the acetaldehyde condensation reaction during gas dosing.

The adsorption is limited by the number of available sites, and it follows that the rate of acetaldehyde adsorption and crotonaldehyde formation during gas dosing can be expressed as

$$\frac{d\theta_A}{dt} = k_A^{ad}(\theta_{sat} - \theta_A - \theta_B) - k_{A\to B}^{DOSE}\theta_A^2, \tag{10}$$

$$\frac{d\theta_B}{dt} = \frac{1}{2}k_{A\to B}^{DOSE}\theta_A^2(\theta_{sat} - \theta_A - \theta_B), \tag{11}$$

where θ_{sat} is the saturation coverage and the factor of ½ in Eq. (11) comes from the stoichiometry relation in reaction (9). Guided by the experimental data, we ignore desorption of acetaldehyde and crotonaldehyde. All acetaldehyde is converted to crotonaldehyde during the purging period. This aldol condensation reaction is strictly a second-order reaction. However, from our *in situ* FTIR data acquired during the gas dosing and purging periods, second-order kinetics was clearly distinguished only during the purging period. Furthermore,

we note that the results from kinetic modelling yielded consistently different rate constants for the condensation reaction ($k_{A\to B}$) during dosing and purging (denoted with superscripts "DOSE" and "PURGE", respectively). A ratio of approximately two for $k_{A\to B}$ in the purging region compared to the situation in the gas dosing region, *i.e.*, of ($k_{A\to B}^{PURGE}/k_{A\to B}^{DOSE}$), was observed throughout the four cycles in our experiments. A probable explanation of this discrepancy is that the reaction is diffusion limited during the dosing period. Such a limitation is also indicated by the much smaller rate constant for adsorption compared to aldehyde oxidation, which is apparent in Table 2.

Table 2. Reaction rate constants $K_{i\to j}$ on TiO_2 obtained from micro-kinetic modelling.

	Rate constant, $\times 10^{-3}$ [μmol·cm^{-2}·s^{-1}]							Quantum yield, $\phi_{i\to j}$ (%)			
Cycle no.	K_A^{ad}	$K_{A\to B}^{DOSE}$	$K_{A\to B}^{PURGE}$	$K_{A\to B}^{UV}$	$K_{B\to C}^{UV}$	K_U^{UV}	K_C^{UV}	$\phi_{A\to B}$	$\phi_{B\to C}$	ϕ_U	ϕ_C
1	0.48	0.526	1.428	0.974	1.495	0.938	0.391	14.6	22.4	14.1	5.9
2	0.617	0.290	0.869	0.526	1.092	0.074	0.257	7.9	16.4	1.1	3.9
3	0.756	0.226	0.521	0.715	1.716	0.118	0.319	10.7	25.7	1.8	4.8
4	0.876	0.252	0.526	0.653	1.613	0.146	0.356	9.8	24.2	2.2	5.3

The adsorption rate constants should therefore be regarded as apparent rate constants, containing both diffusion and adsorption steps. Moreover, since possible minor side-reactions are neglected and absolute coverage calibration for all surface species has not been done (as described in conjunction with Fig. 1), we also enforce the modelled rate constants to absorb these variations. This does, however, not influence the analysis presented here, which primarily aims at quantifying the different photo-induced reaction pathways on TiO_2 and SO_4–TiO_2.

During purging in synthetic air, the aldol condensation reaction continues and, according to the in situ FTIR data, ultimately converts all of the adsorbed acetaldehyde into crotonaldehyde according to

$$2A_{ad} \xrightarrow{k_{A\to B}^{PURGE}} B + H_2O. \qquad (12)$$

The corresponding rate equations are

$$\frac{d\theta_A}{dt} = -k_{A\to B}^{PURGE}\theta_A^2, \tag{13}$$

$$\frac{d\theta_B}{dt} = \frac{1}{2}k_{A\to B}^{PURGE}\theta_A^2(\theta_{sat} - \theta_A - \theta_B). \tag{14}$$

Furthermore, based on the results in Sec. 3.1, we propose that two types of adsorption sites are present on TiO_2, which have different coordination of the aldehyde molecule and obey different reaction kinetics.

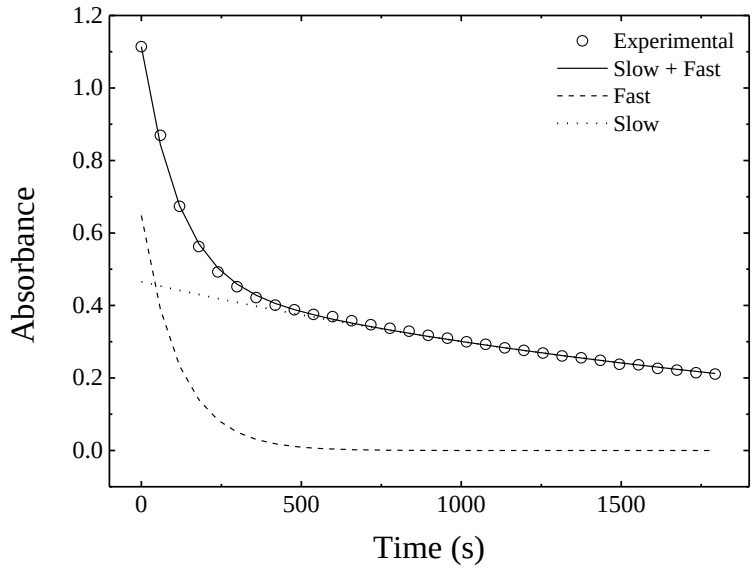

Figure 8. Integrated FTIR absorbance data for the main crotonaldehyde peak on TiO_2 as a function of UV irradiation time. The solid curve is a best fit to the experimental data and comprises of a fast (dashed curve) and slow (dotted curve) first-order degradation reaction.

The existence of two rate constants is particularly evident in the photo-reaction kinetics data. Thus Fig. 8 shows the decay of the crotonaldehydecarbonyl band at 1653 cm^{-1} as a function of UV irradiation time and provides clear evidence for two reaction pathways with very different time-scale. In order to fit the data, the acetaldehyde photo-oxidation is described by

$$C(t) = ZC_0 e^{-k_{B_1} t} + Z'C_0 e^{-k_{B_2} t}, \quad (15)$$

where k_{B_1} and k_{B_2} are the rate constants for the slow and fast reaction, respectively, and Z and Z' are the fractions of each type of species, *i.e.*, $Z + Z' = 1$. Based on their similar kinetic appearance, we assume that two different adsorption sites also are present for acetaldehyde, and that this translates into the kinetic behaviour observed in Fig. 8. Eqs. (13) and (14) are then modified by replacing $k_{A\to B}^{PURGE}$ with $k_{A\to B_1}^{PURGE}$ and $k_{A\to B_2}^{PURGE}$ for the slow and fast acetaldehyde condensation reaction, respectively.

Upon UV irradiation, the following reaction steps are assumed: Crotonaldehydeis first oxidized by radical attack on the C–C bond [11], and subsequent reactions occur in two parallel reaction pathways with different reaction rates, as described by Eq. (15). The major product of this oxidation is formate, which is adsorbed on the TiO_2 surface to form strongly bonded bridging and bidentate species [33]. The formate is then further oxidized to CO_2 and water. For completeness and to account for remaining acetaldehyde on the surface, acetaldehyde monomers species were also included in the model as a possible source of croton aldehyde, *viz*.,

$$2A_{ad} \xrightarrow{k_{A\to B_1}^{UV}} B \xrightarrow{k_{B_1\to C}^{UV}} 4C_{ad} \xrightarrow{k_C^{UV}} CO_2, \quad (16)$$

$$2A_{ad} \xrightarrow{k_{A\to B_2}^{UV}} B \xrightarrow{k_{B_2\to C}^{UV}} 4C_{ad} \xrightarrow{k_C^{UV}} CO_2\ , \quad (17)$$

where *C* is formate. However, the crotonaldehyde coverage can also decrease via other reactions, for example through oxidation to formaldehyde or acetic acid [13, 31, 38]. Even though the latter represent minority surface reaction pathways, meaning that no major IR peaks associated with these species are observed in the experiments, they are nevertheless included in the model to account for mass balance and possible desorption. To extract data for these additional species we have introduced two extra rate constants, one for each of the fast and slow reactions, *viz*.,

$$B_{ad} \xrightarrow{k_{U_1}^{UV},\, k_{U_2}^{UV}} unidentified\ intermediate\ products. \quad (18)$$

Based on the assumptions given above, we arrive at the following overall rate equations for the photo-oxidation of acetaldehyde on TiO_2:

$$\frac{d\theta_A}{dt} = -k_{A\to B_1}^{UV}\theta_A^2 - k_{A\to B_2}^{UV}\theta_A^2, \quad (19)$$

$$\frac{d\theta_B}{dt} = \frac{d\theta_{B_1}}{dt} + \frac{d\theta_{B_2}}{dt}, \quad (20)$$

$$\frac{d\theta_{B_1}}{dt} = \frac{1}{2}k_{A\to B_1}^{UV}\theta_A^2(\theta_{sat} - \theta_A - \theta_B) - k_{B_1\to C}^{UV}\theta_{B_1} - k_{U_1}^{UV}\theta_{B_1}, \quad (21)$$

$$\frac{d\theta_{B_2}}{dt} = \frac{1}{2}k_{A\to B_2}^{UV}\theta_A^2(\theta_{sat} - \theta_A - \theta_B) - k_{B_2\to C}^{UV}\theta_{B_2} - k_{U_2}^{UV}\theta_{B_2}, \quad (22)$$

$$\frac{d\theta_C}{dt} = 4\left(k_{B_1\to C}^{UV}\theta_{B_1} + k_{B_2\to C}^{UV}\theta_{B_2}\right) - k_C^{UV}\theta_C. \quad (23)$$

In the modelling, the experimental data for the crotonaldehydedecomposition are first split into two sets, corresponding to the fast and slow reactions ($k_{X_1}^{UV}, k_{X_2}^{UV}$), before they are fed into the model encapsulated in Eqs. (19) to (23) together with the derived rate constants as an initial guess for the model fitting.

Figure 9(a) shows experimental and simulated results on the temporal evolution of the major surface species as a function of reaction time for the four consecutive cycles of acetaldehyde, involving gas dosing, purging in synthetic air, and UV irradiation. Table 2 presents results of best least-square fits of the model to the absorbance data; for clarity only the sums $k_{A\to B}^{UV} = k_{A\to B_1}^{UV} + k_{A\to B_2}^{UV}$, $k_{B\to C}^{UV} = k_{B_1\to C}^{UV} + k_{B_2\to C}^{UV}$ and $k_U^{UV} = k_{U_1}^{UV} + k_{U_2}^{UV}$ are shown.

Table 3 shows the contributions from the fast and slow reaction steps. It is evident from these results that the reactivity in the first cycle differs significantly from that in the subsequent experimental cycles.

Table 3. Fast and slow reaction rate constants $K_{i\rightarrow j}$ and fractional site occupancies for photo-oxidation of acetaldehyde (on SO_4–TiO_2) and crotonaldehyde(on TiO_2).

TiO_2 surface				
Cycle no.	Sites, %		Rate constant, $\times 10^{-3}$ [μmol·cm^{-2}·s^{-1}]	
	B_1	B_2	$K_{B_1}^{UV}$	$K_{B_2}^{UV}$
1	61.31	38.69	2.04	0.389
2	63.19	36.81	0.95	0.218
3	49.80	50.20	1.59	0.242
4	46.57	53.43	1.32	0.331
SO_4–TiO_2 surface				
Cycle no.	Sites, %		Rate constant, $\times 10^{-3}$ [μmol·cm^{-2}·s^{-1}]	
	A_1	A_2	$K_{A_1}^{UV}$	$K_{A_2}^{UV}$
1	45.68	54.32	2.21	0.907
2	39.04	60.96	1.68	0.835
3	34.26	65.74	1.97	1.07
4	32.69	67.31	2.36	1.33

Although previous reports on rate constants and quantum yield for the individual photo-reactions steps for the photo-oxidation of acetaldehyde on TiO_2 are lacking, our results for the reaction rates and quantum yield in the first reaction cycle 1 shown in Table 2 compare well with the values reported by Kim and Choi [39], and Sopyan et al. [40]. Clearly, the reaction rate decreases after the first cycle, and the formation of side products other than formate is suppressed. It is evident that the reactivity remains approximately unchanged after completion of the first cycle. The formate creation rate is faster than any other surface reaction step, while its degradation rate can be identified as the slow step.

The rate of formate photo-oxidation is not strongly affected by the number of experimental cycles or the decrease of sites associated with the fast degradation reaction pathway (*cf*. Table 3), which confirms that it is the rate-determining intermediate in the photo-oxidation reaction pathway. These results account for the pronounced increase of surface formate as a function of reaction time in Fig. 9. A consequence of the slow formate photo-oxidation is that the number of accessible adsorption sites for acetaldehyde adsorption decreases after the first reaction cycle.

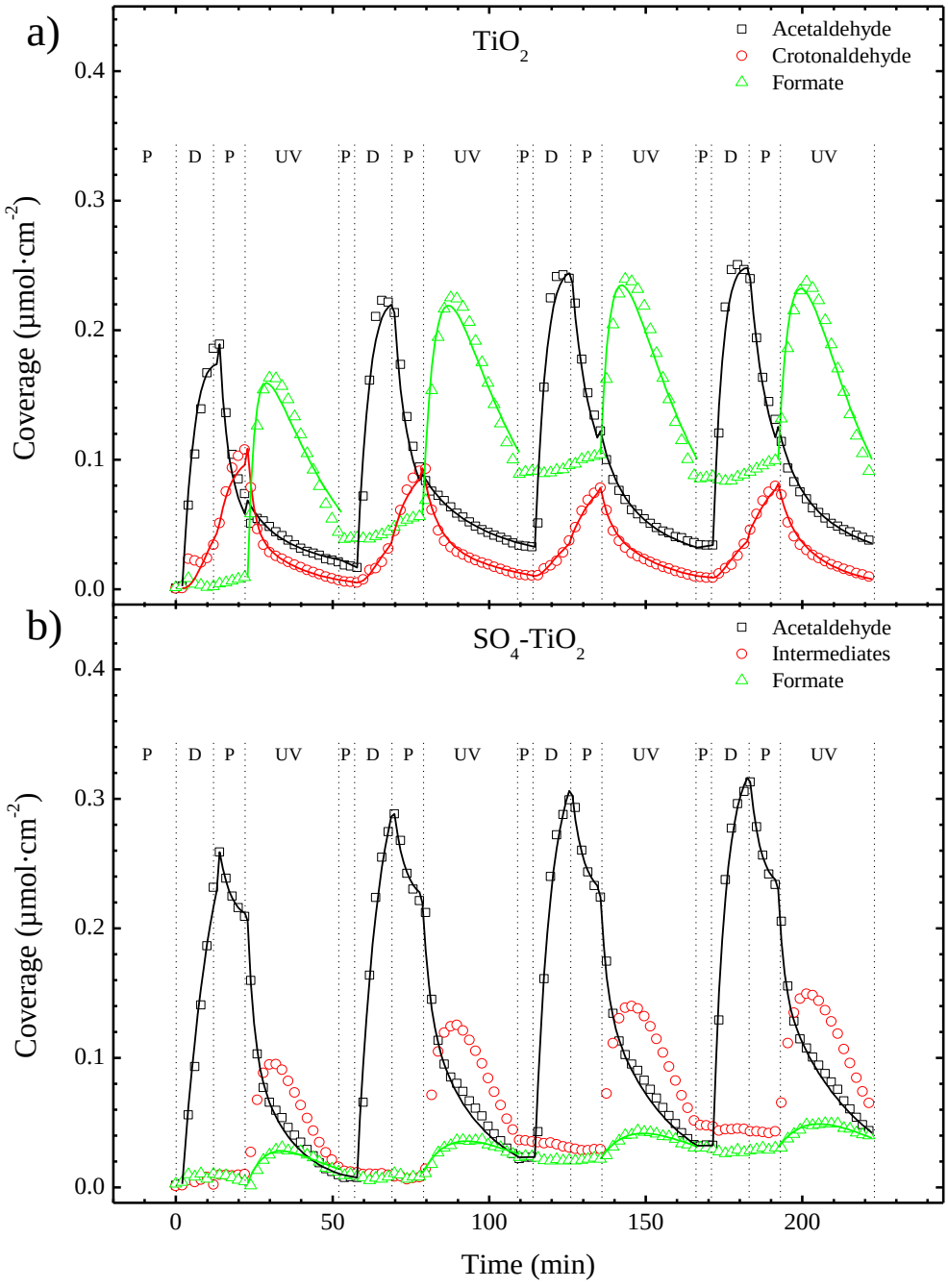

Figure 9. Surface coverage of adsorbed acetaldehyde, crotonaldehyde, and formate as a function of reaction time during four consecutive cycles of acetaldehyde gas dosing (D), purging in synthetic air (P), and UV irradiation (UV), respectively, on (a) TiO_2, and (b) SO_4–TiO_2 films. Solid curves represent results from the micro-kinetic modelling (see text). Note that on SO_4–TiO_2, the unknown carbonyl intermediate surface species (denoted "Intermediates"), which is produced in parallel reactions, was not included in the modelling. The data and simulated results are shown without baseline corrections.

The same conclusion can be drawn from Fig. 7, where the ratio between the formate concentration and initial acetaldehyde concentration increases dramatically in cycle 1, after

which it remains approximately constant. Similarly, the number of sites associated with the fast reaction pathway decreases as a function of cycle number (*cf*. Table 3), which can be interpreted as a consequence of site blocking.

3.3 Reaction kinetics on SO_4–TiO_2

Guided by the experimental data, and by analogy with the results from TiO_2 discussed in Sec. 3.2, we identified the following reaction pathways on SO_4-TiO_2:

$$A_{gas} \xrightarrow{k_A^{ad}} A_{ads} \xrightarrow{k_{A\to C}^{UV}} 2C_{ad} \xrightarrow{k_C^{UV}} CO_2, \quad (24)$$

$$A_{gas} \xrightarrow{k_A^{ad}} A_{ads} \xrightarrow{k_{A\to U}^{UV}} U. \quad (25)$$

The first reaction shows acetaldehyde adsorption and conversion to formate, and reaction (25) describes a parallel reaction of acetaldehyde to an unidentified surface species with its characteristic carbonyl band at 1656 cm^{-1}. The experimental data do not show evidence for aldol reaction prior to UV irradiation and, in contrast to what happens for TiO_2, acetaldehyde desorption is observed on SO_4–TiO_2 as described by

$$A_{gas} \underset{k_A^{des}}{\overset{k_A^{ad}}{\rightleftharpoons}} A_{ads}. \quad (26)$$

Formate is a minor product on SO_4–TiO_2, as shown in Sec. 3.1.2, and the parallel reaction (25) dominates on the surface and is observed during the whole UV illumination period. This surface species is of unknown origin, though, which prevents accurate scaling of the absorbance data as discussed in Sec. 2.4, and hence we have excluded it from the kinetic fitting. For the purpose of comparisons with TiO_2, we therefore focus on the data for formate production and disappearance.

The adsorption kinetics on SO_4–TiO_2 during the dosing period were described by

$$\frac{d\theta_A}{dt} = k_A^{ad}(1-\theta) - k_A^{des}\theta_A, \quad (27)$$

where k_A^{des} is the desorption rate, and k_A^{ad} is the adsorption rate observed during the dosing part. Here the absorbance data were normalized to the saturation coverage, which was estimated by a Langmuir fit as before.

During the purging period only desorption of acetaldehyde takes place, *i.e.*,

$$\frac{d\theta_A}{dt} = -k_A^{des}\theta_A. \quad (28)$$

The acetaldehyde data taken during UV irradiation were split into two data sets and, once again, we used a model with two photo-reaction rate constants corresponding to a fast and a slow reaction pathway. Weighting factors were fitted in order to determine the extent to which each of the reactions affected the total observed rate; data are given in Table 3. The weighting factors correspond to fractions of reaction sites for the pertinent reactions. Finally we used the following set of equations to model the photoreaction:

$$\frac{d\theta_{A_1}}{dt} = k_{A_1\to C}^{UV}\theta_{A_1} - k_{A_1}^{des}\theta_{A_1} - k_{A_1\to U}^{UV}\theta_{A_1}, \quad (29)$$

$$\frac{d\theta_{A_2}}{dt} = k_{A_2\to C}^{UV}\theta_{A_2} - k_{A_2}^{des}\theta_{A_2} - k_{A_2\to U}^{UV}\theta_{A_2}, \quad (30)$$

$$\frac{d\theta_C}{dt} = 2\left(k_{A_2\to C}^{UV}\theta_{A_2} + k_{A_2\to C}^{UV}\theta_{A_2}\right) - k_C^{UV}\theta_C, \quad (31)$$

where θ_{A_1} and θ_{A_2} are the coverages corresponding to the sites for the fast and slow reactions, respectively. Furthermore, $k_{A_{1,2}\to C}^{UV}$ is the rate constant for acetaldehyde-to-formate conversion and $k_{A_{1,2}}^{des}$ is the desorption rate; the sum of these parameters is proportional to the total desorption rate which, in the experiments, was inferred from the peak at 1699 cm^{-1}. The parameter $k_{A_{1,2}\to U}^{UV}$ represents the reaction pathway to the unknown intermediate photo-oxidation product.

Table 4. Reaction rate constants $K_{i\to j}$ on SO_4–TiO_2 as obtained from micro-kinetic modelling.

	Rate constant, $\times 10^{-3}$ [μmol·cm^{-2}·s^{-1}]					Quantum yield, $\phi_{i\to j}$ (%)		
Cycle no.	K_A^{ad}	K_A^{des}	$K_{A\to C}^{UV}$	$K_{A\to U}^{UV}$	K_C^{UV}	$\phi_{A\to C}$	$\phi_{A\to U}$	ϕ_C
1	0.552	1.11	0.132	4.025	1.749	2.0	60.3	26.2
2	0.862	1.07	0.089	3.576	1.133	1.3	53.6	17.0
3	1.12	4.55	0.075	4.460	1.004	1.1	66.9	15.1
4	1.38	4.98	0.076	3.461	1.004	1.1	51.9	15.1

Figure 9b, Table 3 and Table 4 present results from the micro-kinetic modelling on SO_4–TiO_2. Comparing the data in Table 2 with Table 4, one can infer that fast and slow photo-oxidation reactions occur on both TiO_2 and SO_4–TiO_2. The ratio between the fast and slow reaction rates (and quantum yields) is much larger for TiO_2 than for SO_4–TiO_2. Based on the IR spectra, it is natural to assign the two different sites to Lewis Ti^{4+} centres and to acid sites close to surface SO_4^{2-} groups, respectively. We propose that quenching of the fast photo-oxidation pathway on SO_4–TiO_2 is due to interaction with surface SO_4^{2-} groups (Fig. 4), which hinders aldol condensation and leads to acetaldehyde accumulation.

Desorption of acetaldehyde is observed on SO_4-TiO_2, but not on TiO_2, which shows that bonding of acetaldehyde is weaker in the former case. This decrease of the bonding strength might be explained by a protonation mechanism whereby acetaldehyde interacts with surface $HSO_4^{\delta-}$ species (*cf.* Fig. 4), which act as both Lewis and Brönsted acidic sites [41]. Some evidence for two types of sites can be found in the FTIR spectra. As discussed in Sec. 3.1 acetaldehyde adsorption on SO_4–TiO_2 results in a doublet carbonyl band, where the peak at 1684 cm^{-1} is unique for the sulphated TiO_2 and shows that acetaldehyde interacts with the SO_4^{2-} surface species (e.g. structure III in Fig. 4). This is further supported by the concerted disappearance of absorbance bands at ~1340, 1295, and 1110 cm^{-1} in Fig. 3, which previously have been shown to be due to surface coordinated sulphate species on TiO_2 [22], and the appearance of new bands at 1357, 1313, 1221, 1137 and 1097 cm^{-1}.

The collected evidence from our experiments leads us to an explanation for the lack of aldol condensation of acetaldehyde on the sulphated surface as discussed next: We first note that the established mechanism for this reaction [13] involves the carbonyl group of an acetaldehyde molecule, which becomes additionally polarized due to interaction with a Lewis Ti^{4+} centre, and thereby allows for a nucleophilic attack on the carbonyl carbon by another acetaldehyde molecule. Considering SO_4–TiO_2, some of the Lewis acid centres lie close to the electron-rich sulphate groups and therefore allow them to interact with the carbonyl group. This interaction tends to stabilize the structure and thus prevents a nucleophilic attack, thereby hindering aldol condensation. This proposed mechanism can explain both the appearance of the second, intense carbonyl peak at 1684 cm^{-1}, and the modified absorbance in the sulphate region (see Fig. 4).

Comparisons of data in Tables 1 to 3 reveal that the photo-degradation rate and quantum yields remain approximately the same in cycles 1 to 4 on SO_4–TiO_2, while they decrease notably between cycle 1 and 2 on TiO_2 due to accumulation of formate intermediates, as described in Sec. 3.2. The fact that TiO_2 and SO_4–TiO_2 show different performance reflects the variation in the rate-determining reaction step, which is formate photo-oxidation (and CO_2 desorption) in the case of TiO_2 and acetaldehyde photo-oxidation for SO_4–TiO_2. The main difference is that acetaldehyde coordinates to sulphate species on SO_4–TiO_2, which leads to desorption and suppression of formate formation as discussed above. The rate of acetaldehyde photo-oxidation—eventually leading to formate—is smaller than desorption or conversion to other intermediates, and we can thus conclude that SO_4-modification of the acid properties of TiO_2 promotes a higher sustained reactivity of the photocatalysts.

4. Conclusions

Adsorption and photo-oxidation of acetaldehyde on TiO_2 and sulphate-modified TiO_2 films were characterized by in situ FTIR spectroscopy and micro-kinetic modelling. Time-resolved in situ FTIR spectroscopy data provide molecular-level information of the surface reaction kinetics, and provides new insights into the photo-chemistry of aldehydes on TiO_2-based catalysts. It is shown that the selectivity of the surface reactions are modified by the surface sulphate groups on SO_4–TiO_2. Crotonaldehyde formation, which occurs spontaneously on TiO_2 at room temperature, is hindered on SO_4–TiO_2 due to interactions with surface sulphate

groups. Moreover, bonding of aldehyde and carboxylate species is weakened on SO_4–TiO_2, and the formation rate of intermediate formate products is lowered compared to the corresponding rate for TiO_2. Repeated adsorption/photo-oxidation cycles show that the acetaldehyde adsorption capacity is higher on SO_4–TiO_2, which can be explained by a reduced site-blocking effect of strongly bonded formate species which limit the complete oxidation on TiO_2.

The results of the present study show that modifications of the acid-base properties of TiO_2-based photocatalysts can be used to improve their sustained activity. The findings are of considerable interest for a number of applications, where they point towards new strategies to avoid catalyst deactivation and to achieve controlled wetting properties of oxide surfaces for hygienic and medical applications.

Acknowledgments

Financial support was received the European Research Council under the European Community's Seventh Framework Program (FP7/2007-2013)/ERC Grant Agreement No. 267234 ("GRINDOOR"), and from the Swedish Research Council (VR-2010-3514).

References

[1] U. Diebold, Surf. Sci. Rep. 48 (2003) 53.

[2] A. Fujishima, X. Zhang, D.A. Tryk, Surf. Sci. Rep. 63 (2008) 515.

[3] V.A. Henrich, P.A. Cox, The Surface Science of Metal Oxides, Cambridge University Press, Cambridge, 1994.

[4] M.R. Hoffmann, S.T. Martin, W. Choi, D.W. Bahnemann, Chem. Rev. 95 (1995) 69.

[5] A. Mills, J. Wang, M. McGrady, J. Phys. Chem. B 110 (2006) 18324.

[6] G.B. Smith, C.G. Granqvist, Green Nanotechnology: Solutions for Sustainability and Energy in the Built Environment, CRC, Boca Raton, USA, 2010.

[7] P. Wolkoff, C.K. Wilkins, P.A. Clausen, G.D. Nielsen, Indoor Air 16 (2006) 7.

[8] X. Ye, D. Chen, J. Gossage, K. Li, J. Photochem. Photobiol. A 183 (2006) 35.

[9] M.D. Hernández-Alonso, I. Tejedor-Tejedor, M.A. Anderson, J. Soria, Catal. Today 143 (2009) 364.

[10] D.S. Muggli, J.T. McCue, J.L. Falconer, J. Catal. 173 (1998) 470.

[11] R.T. Zehr, M.A. Henderson, Surf. Sci. 602 (2008) 2238.

[12] H. Idriss, M.A. Barteau, Catal. Lett. 40 (1996) 147.

[13] M. Singh, N. Zhou, D.K. Paul, K.J. Klaubunde, J. Catal. 260 (2008) 371.

[14] H. Idriss, C. Diagne, J.P. Hindermann, A. Kiennemann, M.A. Barteau, J. Catal. 155 (1995) 219.

[15] V.V. Ordomsky, V.L. Sushkevich, I.I. Ivanova, J. Mol. Catal. A: Chem. 333 (2010) 85.

[16] A.A. Davydov, Molecular Spectroscopy of Oxide Catalyst Surfaces, Wiley, Chichester, UK, 2003.

[17] G. Ertl, H. Knözinger, J. Weitkamp (Eds.), Handbook of Heterogeneous Catalysis, Wiley-VCH, Weinheim, Germany, 1997.

[18] M.L. Sauer, D.F. Ollis, J. Catal. 163 (1996) 215.

[19] J.N. Armor, Appl. Catal. B 1 (1992) 221.

[20] C. Yanxin, J. Yi, L. Wenzhao, J. Rongchao, T. Shaozhen, H. Wenbin, Catal. Today 50 (1999) 39.

[21] J. Nisar, Z. Topalian, A. De Sarkar, L. Österlund, R. Ahuja, ACS Applied Materials & Interfaces in press.

[22] Z. Topalian, G.A. Niklasson, C.G. Granqvist, L. Österlund, ACS Appl. Mater. Interfaces 4 (2012) 672.

[23] Z. Topalian, G.A. Niklasson, C.G. Granqvist, L. Österlund, Thin Solid Films 518 (2009) 1341.

[24] Powder Diffraction Files, International Center for Diffraction Data, file no. 00–021–1272.

[25] A. Mattsson, M. Leideborg, K. Larsson, G. Westin, L. Österlund, J. Phys. Chem. B 110 (2006) 1210.

[26] Y.J. Kim, M.H. Lee, H.J. Kim, G. Lim, Y.S. Choi, N.G. Park, K. Kim, W.I. Lee, Adv. Mater. 21 (2009) 3668.

[27] T.L. Thompson, J. Yates, Top. Catal. 35 (2005) 197.

[28] R.D.C. Team, R: A language and environment for statistical computing, R Foundation for Statistical Computing, Vienna, Austria, 2011; http://www.R-project.org/.

[29] T. Petzoldt, K. Rinke, J. Stat. Software 22 (2007) 1.

[30] K. Soetaert, T. Petzoldt, R. Woodrow Setzer, J. Stat. Software 33 (2010) 1.

[31] B. Hauchecorne, D. Terrens, S. Verbruggen, J.A. Martens, H.V. Langenhove, K. Demeestere, S. Lenaerts, Appl. Catal. B 106 (2011) 630.

[32] J.E. Rekoske, M.A. Barteau, Langmuir 15 (1999) 2061.

[33] L. Österlund, Vibrational spectroscopy of pure and doped TiO_2 photocatalysts, in: L. Vayssieres (Ed.) On Solar Hydrogen and Nanotechnology, Wiley, Singapore, 2010.

[34] V.P. Indrakanti, J.D. Kubicki, H.H. Schobert, Fuel Process. Technol. 92 (2011) 805.

[35] W. Pipornpong, R. Wanbayor, V. Ruangpornvisuti, Appl. Surf. Sci. 257 (2011) 10322.

[36] E. Obuchi, T. Sakomoto, K. Nakano, F. Shiraishi, Chem. Eng. Sci. 54 (1999) 1525.

[37] W.C. Wu, C.C. Chuang, J.L. Lin, J. Phys. Chem. B 104 (2000) 8719.

[38] D. Kozlov, A.V. Vorontsov, P.G. Smirniotis, E. Savinov, Appl. Catal. B 42 (2003) 77.

[39] H. Kim, W. Choi, Appl. Catal. B, 69 (2007) 127.

[40] I. Sopyan, M. Watanabe, S. Murasawa, K. Hashimoto, A. Fujishima, J. Photochem. Photobiol. A 98 (1996) 79.

[41] Y. Niu, M. Xing, B. Tian, J. Zhang, Appl. Catal. B 115-116 (2012) 253.